Enhancement of UHMWPE encapsulation on the ballistic performance of bi-layer mosaic armors

Zhong-Nan Zhao [a,b,c], Bin Han [b,*], Rui Zhang [a,b,c], Qi Zhang [b], Qian-Cheng Zhang [a], Chang-Ye Ni [c,d], Tian Jian Lu [c,d,**]

[a] State Key Laboratory for Strength and Vibration of Mechanical Structures, Xi'an Jiaotong University, Xi'an, 710049, PR China
[b] School of Mechanical Engineering, Xi'an Jiaotong University, Xi'an, 710049, PR China
[c] State Key Laboratory of Mechanics and Control of Mechanical Structures, Nanjing University of Aeronautics and Astronautics, Nanjing, 210016, PR China
[d] MIIT Key Laboratory of Multifunctional Lightweight Materials and Structures (MLMS), Nanjing University of Aeronautics and Astronautics, Nanjing, 210016, PR China

ABSTRACT

The ballistic performance of a bi-layer armor encapsulated with ultra-high molecular weight polyethylene (UHMWPE) composite laminate was investigated using a combined experimental and numerical approach. Three series of test specimens were examined: (A) bare and encapsulated aluminum (Al) plates, (B) bare and encapsulated bi-layer mosaic armors, and (C) bi-layer mosaic armors having identical areal density but different encapsulation thicknesses. The ballistic behaviors and failure mechanisms of UHMWPE encapsulated Al plates and bi-layer mosaic armors under different projectile impact velocities were analyzed systematically. Attributed to the integration effect of encapsulation, the encapsulated specimens could effectively disperse localized projectile impacting to the entire structure. The results indicated that the UHMWPE encapsulation could enhance significantly the ballistic resistance of traditional ceramic/metal bi-layer armors, due mainly to serious pulling and stretching deformations of the lateral and rear UHMWPE laminates in resisting the projectile impact. However, thicker encapsulation would not necessarily lead to better ballistic performance for specimens with equal areal density. Further, the thickness (or mass) ratio of the armor substructures needed to be tailored synthetically to achieve optimal ballistic performance.

1. Introduction

Improving combat survivability continues to be one of the most important aspects for military applications. To this end, in lieu of traditional metallic armors, high-performance lightweight armor systems, such as ceramic/metal bi-layers that combined the advantages of multiple material properties, were widely exploited for protecting human body and civil/military equipment (e.g., vehicles and helicopters) against projectile impact.

In early studies, Wilkins [1,2] evaluated the ballistic performance of alumina/aluminum bi-layer armors. Subsequently, ceramic-based armor systems were extensively studied worldwide. Typically, a ceramic-based armor consisted of a striking ceramic plate which initially defeated, deformed and eroded the projectile, and a backing metal plate

which supported the striking plate and absorbed the remaining kinematic energy of the penetrating projectile [3–5]. To further enhance the ballistic resistance of ceramic/metal bi-layer armors, a variety of approaches had been attempted, including optimizing the thickness ratio of ceramic to metal [6,7], choosing stronger ceramics [8], ceramic modification [9], arranging ceramic tiles in a mosaic pattern [10], and using metal lattice frame as supporting plate [11–13].

Recently, a large number of advanced fiber-reinforced composites had been developed for superior ballistic resistance, including carbon fiber composites [14,15], aramid fiber composites (e.g., Kevlar, Twaron) [16–18], and ultra-high molecular weight Polyethylene (UHMWPE) fiber composites (e.g., Dyneema, Spectra) [19–23]. In particular, UHMWPE composite laminates with a [0°/90°] cross-ply architecture were increasingly employed for their high resistance to penetration and
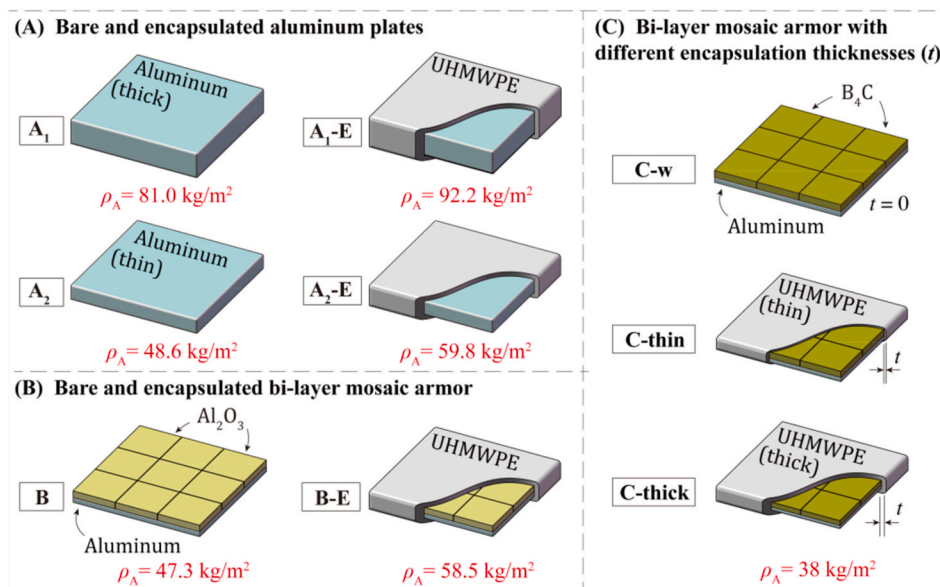
Fig. 1. Sketches of three different armor series: (A) bare and encapsulated aluminum plates, (B) bare and encapsulated bi-layer mosaic armors, and (C) bi-layer mosaic armors with different encapsulation thicknesses. For mosaic armors, 50 mm wide ceramic tiles were arranged in a 3 × 3 pattern. Series C specimens had identical areal density.

low density [24–26]. It was further shown that the UHMWPE laminates should be combined with bulletproof materials of high hardness due to the limited protective capability of a single UHMWPE plate [27–32]. It was therefore envisioned that the ballistic resistance of a traditional ceramic/metal bi-layer armor could be greatly elevated by combing it with UHMWPE laminate to construct a new armor system without adding significant weight. Nevertheless, how to bond the UHMWPE laminate with the bi-layer armor became a critical issue. Thus far, free stacking and bolted clamping were two commonly used connecting methods, but both exhibited deficiencies:

(i) With bolted clamping, serious stress concentration occurred around the bolt holes. The low friction coefficient and large deformation of UHMWPE laminates made it difficult to clamp the target and grasp the laminates with other materials upon impact. In addition, premature failure occurring at bolt holes led to inferior ballistic resistance [14,20].

(ii) With free stacking, there was no connection between the UHMWPE laminate and other components of the armor. As a result, a portion of the laminate would eventually separate from the target and move together with the projectile. In other words, several layers of the laminate were not involved in absorbing the impact energy and hence did not contribute to the ballistic resistance [33,34].

To address these deficiencies, a self-fixation method of UHMWPE laminate was proposed [35,36], that is, an alternative wrapping technique was applied to enhance the ballistic performance of aluminum and alumina-aluminum plates. These targets encapsulated by UHMWPE laminate via the wrapping technique were found to exhibit a much higher ballistic limit, albeit compromised by somewhat increase in areal density. Subsequently, based upon the method of finite elements (FE), Zhang et al. [34] conducted a numerical study to explore the physical mechanisms underlying the superior performance of UHMWPE encapsulated targets. At present, the enhancement effect of UHMWPE encapsulation had been confirmed only for aluminum and alumina-aluminum plates. For other armor systems, especially bi-layer mosaic armors, the projectile penetration processes and enhancement mechanisms of UHMWPE encapsulation remain elusive.

The present work aims to characterize the ballistic performance of

UHMWPE encapsulated aluminum plates and ceramic/metal bi-layer armors and explore the underlying physical mechanisms, both experimentally and numerically. Meanwhile, from the viewpoint of armors having equal mass, encapsulated ceramic/metal bi-layer armors with varying material mass ratios are systematically analyzed for the first time. The work is structured as follows. Section 2 will describe the problem and introduced three different series of specimens investigated in this study. In Section 3, details of the fabrication method for test specimens and the ballistic tests will be presented, and the responses measured under sphere projectile impact will be described and contrasted. In Section 4, three-dimensional (3D) finite element (FE) models will be established and validated against test results. Finally, in Section 5, observations from the 3D FE simulations will be assembled to elucidate the enhancement mechanisms and the influence of key factors (e.g., impact velocity and substructure mass ratio).

2. Problem description

As shown in Fig. 1, three series of armor specimens were investigated to uncover the enhancement mechanisms of UHMWPE encapsulation. For the brevity, in series A and B, the bare (un-encapsulated) specimens were labeled as A_1, A_2 and B, while the encapsulated specimens were labeled as A_1-E, A_2-E and B-E, with E denoting encapsulation. In series C, the specimens without encapsulation, with thin encapsulation, and with thick encapsulation were labeled as C-w, C-thin and C-thick, respectively. Details of the three series were summarized, as follows:

(A) Bare and encapsulated aluminum plates: this series included two bare and encapsulated Al 6061-T6 plates with different plate thicknesses, i.e., A_1 and A_2. The A_1 and A_2 plates were 30 mm and 18 mm thick, respectively. When encapsulated with a 5.9 mm thick UHMWPE laminate, the specimens became A_1-E and A_2-E. Their corresponding areal densities were present in Fig. 1.

(B) Bare and encapsulated bi-layer mosaic armor: this series comprised a bare alumina/aluminum plate with mosaic ceramics (i.e., B) and an encapsulated one (i.e., B-E). In the mosaic armor, square Al_2O_3 tiles with a width of 50 mm were arranged in a 3 × 3 pattern. The thickness of each Al_2O_3 tile and that of the Al 6061-T6 backing plate were 8 mm and 6 mm, respectively. Same as in series A, the encapsulation of specimen B-E was also 5.9 mm
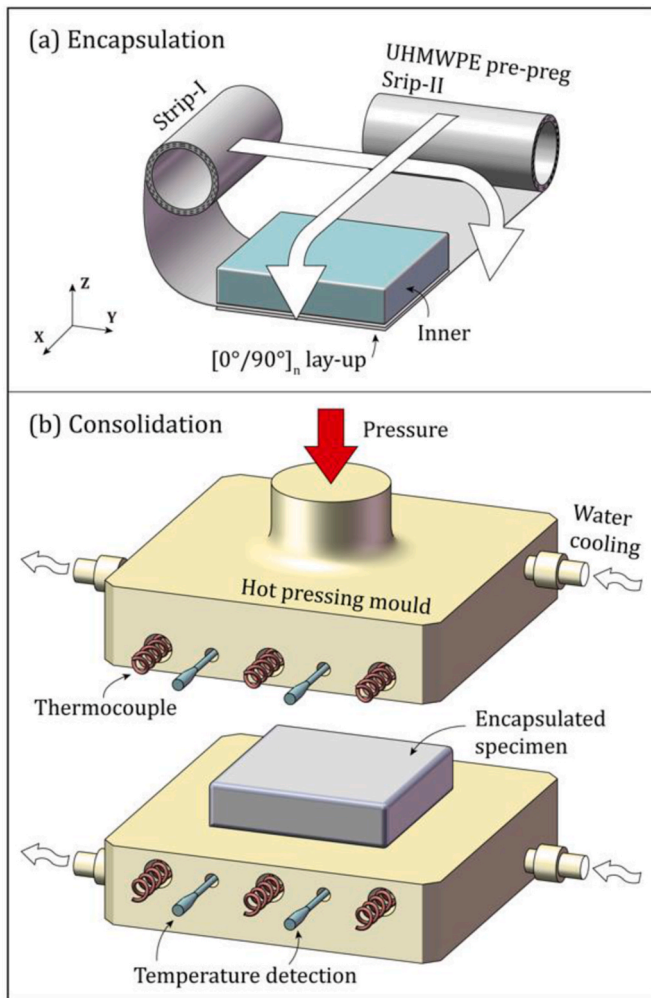
Fig. 2. Two-step fabrication process of armor encapsulation, with specimen A_1-E shown for illustration.

thick. Additionally, to facilitate subsequent comparisons, the areal densities of specimens A_2 and B were approximate equal, so were A_2-E and B-E.

(C) Bi-layer mosaic armors having different encapsulation thicknesses: specimens with 0, 2.3 mm, 5.9 mm thick encapsulation were comprised in this series, but with the areal density of each specimen fixed at 38 kg/m². Thus, three typical encapsulated structures were considered, *i.e.*, no encapsulation, thin encapsulation, and thick encapsulation, labeled below as C-w, C-thin, and

C-thick. It should be noticed that, for this series of armors, the Al_2O_3 ceramic tiles and the Al 6061-T6 backing plate were separately replaced by B_4C and Al 7075-T6 for improved ballistic performance at a lower areal density.

3. Impact tests and characterization

3.1. Materials and fabrication

For series A armors, Al 6061-T6 alloy, yield strength 324 MPa, was selected as the parent material of metal plates. For series B, AD995 alumina (Al_2O_3), density 3.89 g/cm³, and Al 6061-T6 were employed as the front and back plate, respectively. For series C, Al_2O_3 ceramic and Al 6061-T6 were replaced by B_4C (density 2.51 g/cm³) and Al 7075-T6 (yield strength 546 MPa), for enhanced ballistic performance at lower areal density. Armor encapsulation was achieved with UHMWPE laminate (commercial designation Dyneema® HB26). The ceramic was supplied in the form of square tiles, 50 mm × 50 mm in size. A two-component epoxy adhesive was used to bond the ceramic tiles and the backing plate. In-plane dimensions of all the specimens were fixed at 150 mm × 150 mm.

Fig. 2 displayed schematically the manufacturing process for UHMWPE encapsulated armors:

(a) Two strips of UHMWPE pre-preg tape (with a stacking sequence of $[0°/90°]_2$, each layer ~0.27 mm thick) were cut along the 0°/90° fiber orientation. The original bare armor was then alternatively wrapped by each UHMWPE pre-preg strip to form a $[0°/90°]_{2n}$ lay-up. For specimens with 5.9 mm encapsulation thickness (all specimens in series A and B, C-thick in series C), the HB26 pre-preg strip I and II was alternatively wrapped around the bare armor eleven times. The lay-up from on both the front and rear faces was $[(0/90)_2/(0/90)_2]_{11} = [0°/90°]_{2(22)} = [0°/90°]_{44}$ with a thickness of 5.9 mm. The lay-up on four lateral faces was $[0/90]_{22}$ and thus only half the thickness of that on the front and rear faces. In comparison, the front and rear encapsulation of $[0°/90°]_{36}$ lay-up and the lateral encapsulation of $[0°/90°]_{18}$ lay-up led to a 2.3 mm thick UHMWPE encapsulation. It is worth noting that, the encapsulation thicknesses were measured and averaged after consolidation, so there was an error compared with the theoretical value (<5%).

(b) Encapsulated specimens were consolidated via a hot pressing mold equipped with a water cooling system. The consolidation consisted of 4 steps. (i) Pre-heating: before consolidation, the hot pressing mold was pre-heated to ~110 °C and the specimen was heated without pressure for 10 min; (ii) Heating and pressurization: the pressure and temperature were set to 20 MPa and 125 °C, lasting for about 20 min; (iii) Cooling and pressure-holding: heating was stopped and the water cooling system started to
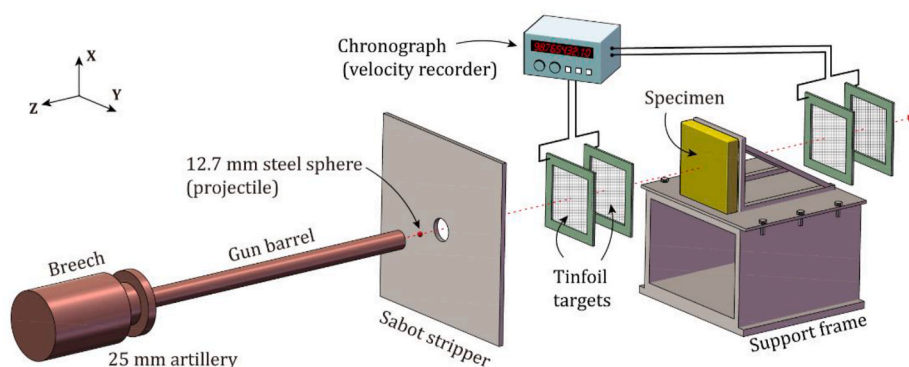

Fig. 3. Schematic illustration of the ballistic testing system.

Table 1
Summary of ballistic tests performed on series A and B specimens.

Series	Specimen	t (mm)[a]	ρ_A (kg/m^2)	V_i (m/s)	N/P[b]
A	A$_1$	–	81.0	936.8	N
				992.0	N
				1187.5	P
	A$_1$-E	5.9	92.2	1092.2	N
				1284.3	N
				1341.0	P
				1365.2	P
				1403.8	P
				1535.2	P
	A$_2$	–	48.6	700.3	N
				776.1	P
				877.6	P
				945.4	P
	A$_2$-E	5.9	59.8	838.7	N
				971.9	N
				1260.6	P
B	B	–	47.3	806.4	N
				885.1	P
				1130.3	P
	B-E	5.9	58.5	1424	N
				1467	N
				1529	P
				1612	P

[a] t: Encapsulation thickness.
[b] N: Not perforated. P: Perforated.

work, while the pressure was maintained at 20 MPa; (iv) Unloading: when the specimen temperature dropped to 60 $^\circ$C, the mold was unloaded and the whole consolidation process finished.

3.2. Impact test protocol

Ballistic tests were performed with a 25 mm artillery, as shown in Fig. 3. AISI 4340 steel sphere, diameter 12.7 mm and weight 8.4 g, was used as the striking projectile, with its initial lunching velocity varied in the range of 700–1700 m/s. For easy and quick comparison, whether penetration across a specimen occurred was employed as the performance test standard in series A and B. While for series C, to evaluate the enhancement of UHMWPE encapsulation for mosaic armors under different impact velocities, both the initial and residual projectile velocities were recorded with tinfoil targets. A sabot stripper plate was employed to separate the projectile from the launching sabot before impacting the target. The distance between the tinfoil targets and the specimen was about 500 mm to avoid the debris. A support frame made of mild steel was employed to clamp each specimen during the tests. Specimens were mounted in a simply supported boundary condition,

with four corners fixed on the support frame using cast iron clamps.

3.3. Experimental results

The areal density ρ_A, initial impact velocity V_i and residual velocity V_r of all specimens were listed in Table 1 (Series A and B) and Table 3 (Series C). In order to facilitate the comparison of how the ballistic limit velocity (BLV) varied for series A and B, the data of Table 1 was used to construct Table 2. In Table 2, the effect of encapsulation enhancement was characterized using the ballistic limit velocity BLV, the area density ρ_A, and their variations ΔBLV and $\Delta\rho_A$. Additionally, the ratio of ΔBLV and $\Delta\rho_A$ was utilized to quantify the encapsulation enhancement per area density.

3.3.1. Series A and B
Based on the experimental data, 7 groups of comparison were listed in Table 2. Groups 1–3 compared the bare and the encapsulated specimens; Groups 4 and 5 compared the bare and the encapsulated Al plates having different plate thicknesses; Group 6 compared the bare Al plates and the Al$_2$O$_3$/Al bi-layer plates having identical areal density, while Group 7 compared the encapsulated Al plates and the Al$_2$O$_3$/Al bi-layer plates.

(i) The results of Groups 1–3 showed that UHMWPE encapsulation could improve the ballistic performance of both the Al plates and the Al$_2$O$_3$/Al bi-layer plates. However, with the thickness of UHMWPE encapsulation fixed at 5.9 mm, the increase in BLV was different. For the Al plates, both thick and thin, the encapsulation increased the BLV by $\sim$280 m/s (or, equivalently, $\sim$25 m/s per

Table 3
Summary of ballistic tests performed on Series C specimens.

Series	Specimen	t (mm)[a]	ρ_A (kg/m^2)	V_i (m/s)	V_r (m/s)
C	C-w	–	38.3	932.1	0
				1178.1	386.2
				1270.4	483.8
	C-thin	2.3	38.7	1035.1	0
				1056.4	0
				1131.8	0
				1277.6	0
				1329.3	383.9
				1382.5	541.6
				1477.2	682.4
	C-thick	5.9	38.9	958.1	0
				1179.5	527.5
				1284.4	605.8
				1320.7	679.1

[a] t: Encapsulation thickness.

Table 2
Comparisons among series A and B specimens.

No.	Specimen	BLV[a] (m/s)	ρ_A(kg/m^2)	ΔBLV(m/s)	$\Delta\rho_A$(kg/m^2)	$\frac{\Delta BLV}{\Delta\rho_A}$(m^3/(s·kg))	$\frac{\Delta BLV}{BLV}$
1	A$_1$	992	81	292.3	11.2	26.10	29.47%
	A$_1$-E	1284.3	92.2				
2	A$_2$	700.3	48.6	271.6	11.2	24.25	38.78%
	A$_2$-E	971.9	59.8				
3	B	806.4	47.3	660.6	11.2	58.98	81.92%
	B-E	1467	58.5				
4	A$_2$	700.3	48.6	291.7	32.4	9.00	41.67%
	A$_1$	992	81				
5	A$_2$-E	971.9	59.8	312.4	32.4	9.64	32.10%
	A$_1$-E	1284.3	92.2				
6	A$_2$	700.3	48.6	106.1	1.3	81.62	15.15%
	B	806.4	47.3				
7	A$_2$-E	971.9	59.8	495.1	1.3	380.85	50.94%
	B-E	1467	58.5				

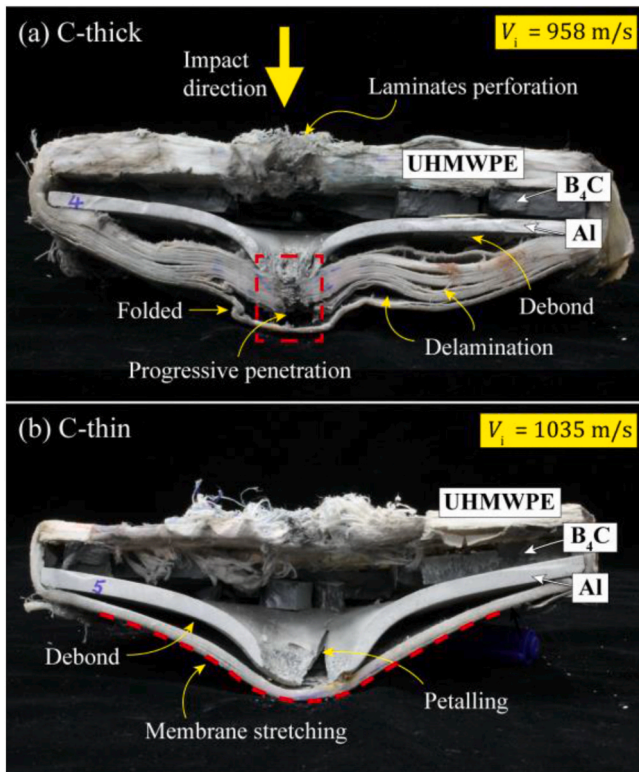[a] BLV: ballistic limit velocity, corresponding to the lowest perforation speed.

Fig. 4. Transverse cross-sections of unperforated (a) C-thick and (b) C-thin specimens upon spherical projectile impact at about 1000 m/s.
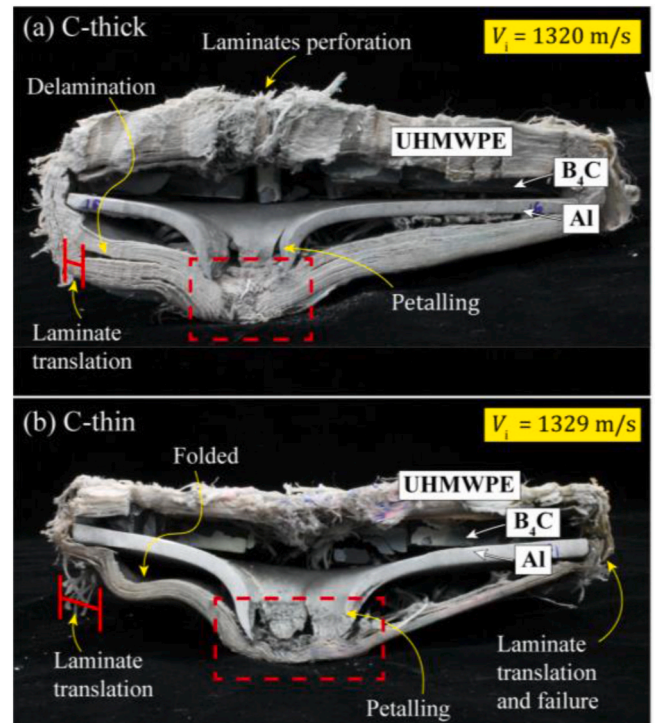

Fig. 5. Transverse cross-sections of perforated (a) C-thick and (b) C-thin specimens after spherical projectile impact at about 1300 m/s.

area density). While for the Al_2O_3/Al plates with the same encapsulation, the BLV was elevated to 660.6 m/s (or 58.98 m/s per area density).

(ii) From Groups 1–2 and 4–5, it could be concluded that as the Al plate thickness was increased, the increases in BLV for both the bare and encapsulated specimens were almost the same. In other words, with identical UHMWPE encapsulation, both the thin and thick Al plates exhibited similar enhancement in ballistic resistance.

(iii) Specimens with similar areal densities were compared in Groups 6 and 7. The results indicated that the BLV of the bare Al_2O_3/Al bi-layer (B) exceeded that of the Al plate (A_2), with an increase of about 100 m/s; while an increase of nearly 500 m/s in BLV was achieved by the encapsulated Al_2O_3/Al plate (B-E) in comparison with that of the encapsulated Al plate (A_2-E). This suggested that UHMWPE encapsulation greatly enlarged the superiority of Al_2O_3/Al bi-layer armor in ballistic resistance.

In summary, although the use of UHMWPE encapsulation could elevate the BLV of armor, the type of armor (e.g., Al plate versus Al_2O_3/Al bi-layer) greatly affected the enhancement of encapsulation: the Al_2O_3/Al bi-layer exhibited a superior ballistic resistance relative to the Al plate of identical areal density. Therefore, the role of UHMWPE encapsulation was further experimentally investigated in Series C, as reported below.

3.3.2. Series C

Different from Specimen B, Specimen C was comprised of B_4C ceramic tiles and an Al 7075-T6 backing plate, thus achieving a considerably lower areal density. Table 3 listed the experimental results of without encapsulation (C-w), thin encapsulation (C-thin) and thick encapsulation (C-thick) specimens, with their areal densities fixed at ~38.5 kg/m². The ballistic performance increased in order, *i.e.*, C-thick, C-w and C-thin, with C-thin achieving the highest BLV (i.e., highest

ballistic resistance). This implied that a thicker encapsulation did not necessarily lead to enhanced ballistic resistance, as the armor having a suitable substructure mass ratio exhibited the best performance. Therefore, for optimal ballistic performance, the thicknesses of encapsulation, ceramic tiles and aluminum plate needed to be comprehensively considered, which would be systematically investigated in Section 5 via numerical simulations.

As depicted in Fig. 4, both the C-thick and C-thin specimens were unperforated under projectile strike at a similar speed of ~1000 m/s; the cross-section image displayed for each specimen was obtained upon applying the high-pressure water-jet cutting technology. Similarities between the two specimens in deformation and failure modes were abundant. The B_4C ceramic tile beneath the impact position was crushed and washed away during water-jet sectioning, while the surrounding ceramic tiles exhibited considerably lower degree of damage, with a few still bonded to adjacent ones. Obvious debonding occurred between the Al plate and the rear UHMWPE laminate in each specimen, but their deformation and failure modes were quite different. As shown in Fig. 4a for the C-thick specimen, the rear UHMWPE laminate experiences serious delamination and progressively localized breakage of its sub-layers. The specimen was almost completely perforated. Differently as shown in Fig. 4b, almost all the sub-layers of the rear UHMWPE laminate were intact in the C-thin specimen, and the whole laminate exhibited an integral stretching deformation (*i.e.*, membrane stretching). Further, the Al plate exhibited a localized plugging failure in C-thick, but presented a typical petaling failure in C-thin.

Fig. 5 displayed the transverse cross-sections of two fully perforated specimens, after projectile impact at about 1300 m/s. The rear UHMWPE laminate was transversely deflected while the lateral UHMWPE was strongly deformed by pulling, demonstrating vividly the contribution of encapsulation to ballistic resistance. UHMWPE encapsulation not only prevented boundary separation, but also integrated different parts of the armor. Note however two differences: (1) the lateral UHMWPE part of the C-thin began to fail at corners, which was related to the strength of the lateral UHMWPE and would be discussed later in Section 5.2; (2) the deformation region of the Al plate and rear
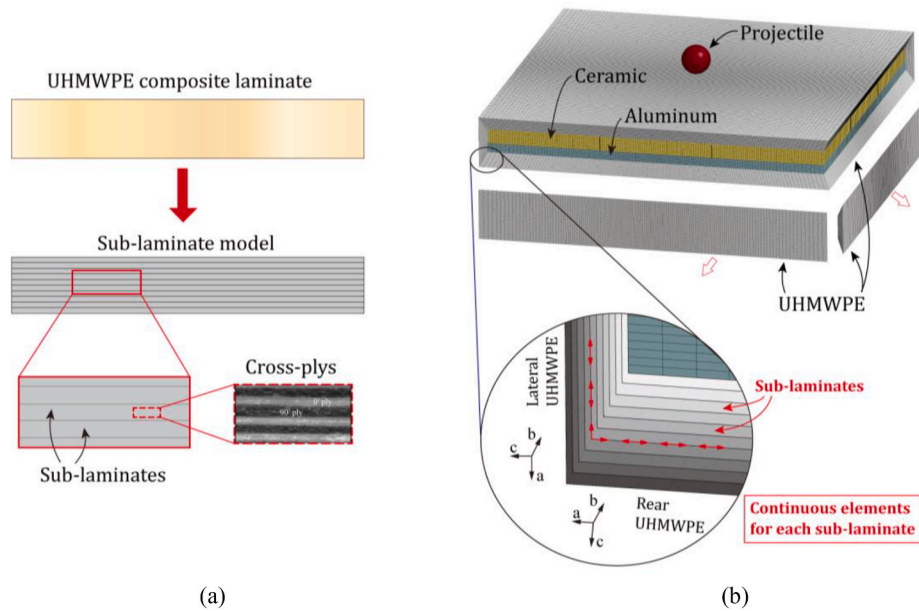
(a)   (b)

Fig. 6. (a) Schematic of sub-laminate model for UHMWPE composite laminate, (b) numerical models for encapsulated specimen (taking C-thick for example, referred to Fig. 1). Magnified view showed continuous elements of each sub-laminate between lateral and rear UHMWPE encapsulations.

UHMWPE laminate in C-thin were larger than that in C-thick (see the red frame in Fig. 5), which meant that the constituent materials of the former dissipated much more energy. This exactly reflected the difference in their performances shown in Table 3.

4. Numerical simulations

4.1. Finite element model

Numerical simulations based upon the finite element method (FEM) were performed with the commercial software LS-DYNA. The UHMWPE encapsulation was discretized into sub-laminates to form multiple sub-layers across its thickness. Previous studies demonstrated the applicability of this sub-laminate model in predicting the out-of-plane deformation of UHMWPE laminate [33,34,37]. The UHMWPE laminate was assumed to be orthotropic, consisting of several sub-layers which were joined together, as shown in Fig. 6a. Each sub-layer (referred as sub-laminate) could be considered as a homogenization of several thin cross-plies. Based on this assumption, the actual interfaces in the UHMWPE laminate were reduced to interfaces between adjacent sub-laminates. Delamination could be simulated by defining failure between adjacent sub-laminates.

Fig. 6b displayed the three-dimensional (3D) sub-laminate model for the present UHMWPE encapsulated specimens (taking C-thick as example), with 3D reduced integration solid elements used to mesh each sub-structure of the specimen. Although sharp edges would change the failure mode of UHMWPE laminate, and will be points of enhanced tension and failure [38], the chamfers on plate edges had little effect on the ballistic performance. For simplicity and to ensure the stability of numerical simulations, the chamfers on plate edges and the epoxy adhesive used to bond the ceramic tiles and the backing plate were neglected in the FE model. For balanced numerical convergence and computational cost, the thickness of the sub-laminate was set as 0.66 mm, which corresponded to an UHMWPE laminate with $[0°/90°]_5$ layer-up. A global mesh size of 0.5 mm was used for the spherical projectile. The Al plate was meshed with element size varying from 0.5 mm to 2.2 mm. The central ceramic tile directly under impact was meshed with an element size 0.5 mm, while the side ceramic tiles were meshed using an element size of 1 mm. The mesh size of the UHMWPE was 0.5 mm along the in-plane direction and 0.66 mm in the thickness direction.

The 0.66 mm sub-laminate corresponded to a HB26 laminated plate with configuration $[0°/90°]_5$. The region directly beneath projectile impact was modeled with relatively dense meshes to capture projectile penetration details. Mesh sensitivity study was carefully carried out (details not shown here for brevity), which ensured that the mesh sizes presented above ware sufficient for numerical convergence.

4.2. Material models

The materials employed in the simulation include UHMWPE composite laminate, AISI 4340 steel, Al 6061-T6, Al 7075-T6, and B_4C ceramic.

The HB26 UHMWPE laminate was assumed to be orthotropic, and was modeled by a composite material model with failure criterion (MAT_COMPOSITE_FAILURE in LS-DYNA). Its linear elastic relation between stress and strain was described as:

$$\begin{Bmatrix} \varepsilon_a \\ \varepsilon_b \\ \varepsilon_c \\ \gamma_{bc} \\ \gamma_{ca} \\ \gamma_{ab} \end{Bmatrix} = \begin{Bmatrix} \frac{1}{E_a} & -\frac{\nu_{ba}}{E_b} & -\frac{\nu_{ca}}{E_c} & 0 & 0 & 0 \\ -\frac{\nu_{ab}}{E_a} & \frac{1}{E_b} & -\frac{\nu_{cb}}{E_c} & 0 & 0 & 0 \\ -\frac{\nu_{ac}}{E_a} & -\frac{\nu_{bc}}{E_b} & \frac{1}{E_c} & 0 & 0 & 0 \\ 0 & 0 & 0 & \frac{1}{G_{cb}} & 0 & 0 \\ 0 & 0 & 0 & 0 & \frac{1}{G_{ca}} & 0 \\ 0 & 0 & 0 & 0 & 0 & \frac{1}{G_{ab}} \end{Bmatrix} \begin{Bmatrix} \sigma_a \\ \sigma_b \\ \sigma_c \\ \tau_{bc} \\ \tau_{ca} \\ \tau_{ab} \end{Bmatrix} \quad (1)$$

where E was the elastic modulus, G was the shear modulus and ν was the Poisson ratio; the subscripts a, b, and c denoted local element axes. As for the failure modes, the in-plane tensile strengths and the out-of-plane compressive strength were defined. The maximum tensile strain was set as 0.4, while the compressive volumetric strain was 0.8 to eliminate failed elements. Strain rate effect and thermal softening of UHMWPE material were ignored in the current numerical model. Tiebreak contacts between adjacent sub-laminates were employed to simulate delamination failure, defined as:

Table 4
Material parameters for HB26 UHMWPE laminate [34].

Elastic properties			Strength and failure	
Young's modulus, E_a (GPa)	34.257		Tensile strength, T_a (GPa)	1.25
Young's modulus, E_b (GPa)	34.257		Tensile strength, T_b (GPa)	1.25
Young's modulus, E_c (GPa)	3.26		Compressive strength, C_c (GPa)	1.9
Poisson's ratio, ν_{ba}	0			
Poisson's ratio, ν_{ca}	0.013			
Poisson's ratio, ν_{cb}	0.013			
Shear modulus, G_{ab} (GPa)	0.1738		*Sub-laminate interface strength*	
Shear modulus, G_{ca} (GPa)	0.5478		Normal strength, I_n (MPa)	1.2
Shear modulus, G_{cb} (GPa)	0.5478		Shear strength, I_s (MPa)	2.6

Table 5
Material parameters for 4340 steel [39], Al 6061-T6 [41] and Al 7075-T6 [40].

Materials	Steel 4340	Al 6061-T6	Al 7075-T6
Density, ρ (g/cm^3)	7.7	2.7	2.8
Shear modulus, G (GPa)	77	27.6	26.7
Static yield strength, A (GPa)	0.792	0.324	0.546
Strain hardening constant, B (GPa)	0.0051	0.114	0.678
Strain hardening exponent, n	0.26	0.42	0.71
Strain rate constant, C	0.014	0.002	0.024
Thermal softening exponent, m	1.03	1.34	1.56
Melting temperature, t_m (K)	1793	893	946
Specific heat, C_r (J/kg·K)	477	885	848

Table 6
Material parameters for B$_4$C ceramic [42].

Parameter	B$_4$C
Density, ρ (g/cm^3)	2.51
Shear modulus, G (GPa)	197
Pressure constant, K_1 (GPa)	233
Pressure constant, K_2 (GPa)	−593
Pressure constant, K_3 (GPa)	2800
Bulking factor, β	1.0
Hugoniot elastic limit (*HEL*) (GPa)	19.0
Intact strength constant, A	0.927
Intact strength constant, n	0.67
Strain rate constant, C	0.005
Fracture strength constant, B (GPa)	0.70
Fracture strength constant, m	0.85
Hydrostatic tensile limit, T (GPa)	0.26
Damage constant, D_1	0.001
Damage constant, D_2	0.5

$$\left(\frac{\sigma_n}{I_n}\right)^2 + \left(\frac{\sigma_s}{I_s}\right)^2 \geq 1 \tag{2}$$

where σ_n and σ_s were the normal and shear stresses; I_n and I_s were the normal and shear failure strengths. Corresponding material parameters were listed in Table 4.

The AISI 4340 steel, Al 6061-T6 and 7075-T6 were modeled using the Johnson-Cook material model, with corresponding material parameters listed in Table 5. For B$_4$C ceramic, the Johnson-Holmquist-2 constitutive relation and damage criterion were adopted. Relevant parameters taken from Refs. [39–42] were listed in Table 6.

4.3. Validation against experimental measurements

To validate the FE models, numerical results calculated for both the bare and encapsulated aluminum plates (*i.e.*, Series A) were compared
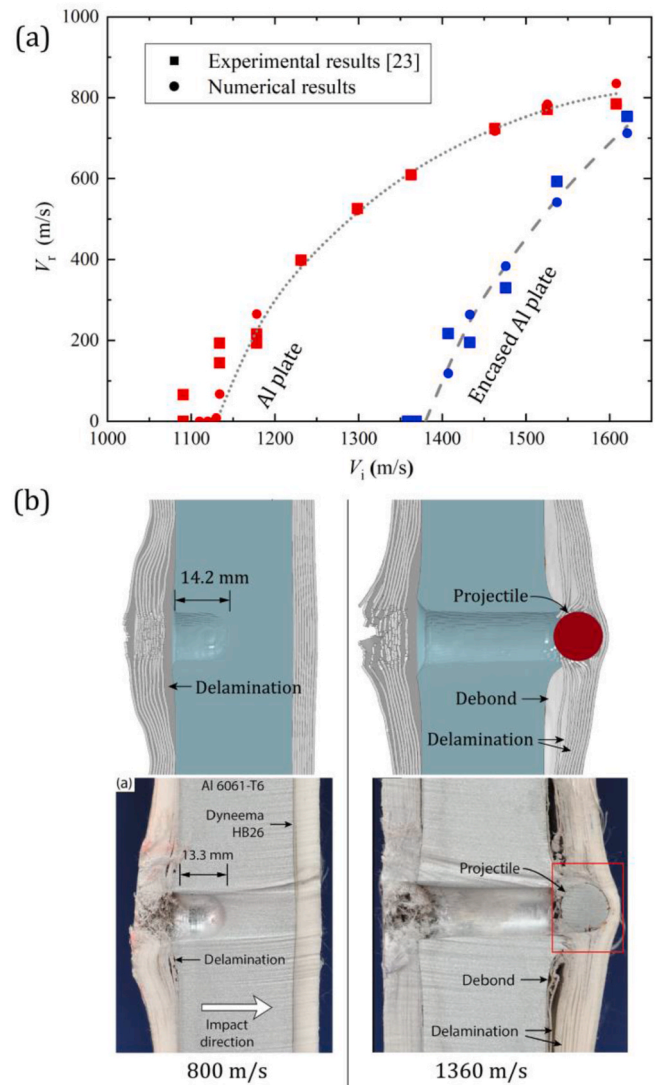

Fig. 7. Comparison between experimental measurements [35] and numerical predictions of both (a) residual velocities and (b) transverse cross-sections for the encapsulated 31.6 mm aluminum plates impacted by a 12.7 mm steel sphere.

with existing experimental results [35]. As shown in Fig. 7a, the numerically calculated residual velocities were in good agreement with test data. Moreover, as shown in Fig. 7b, when the impact velocity reached 800 m/s (less than the BLV), the FE model correctly predicted that only the front UHMWPE and the Al plate were penetrated, with a prediction error of 6.8% for the penetration depth. When the impact velocity was increased to 1360 m/s (near the BLV), the projectile stopped after penetrating a certain distance into the rear UHMWPE. The numerically calculated deformation and failure modes of the considered targets also agreed well with experimental observations.

As for the encapsulated B$_4$C/Al bi-layer mosaic armors (*i.e.*, C-w, C-thin and C-thick), comparison between numerical and experimental results was presented in Fig. 8. Again, good agreement was achieved for enhanced B$_4$C/Al armors having different encapsulation thicknesses.

In conclusion, the feasibility and validity of the present FE models was guaranteed.

5. Results and discussion

Numerical calculations using the validated FE models were carried out to explore the enhancement mechanisms of UHMWPE
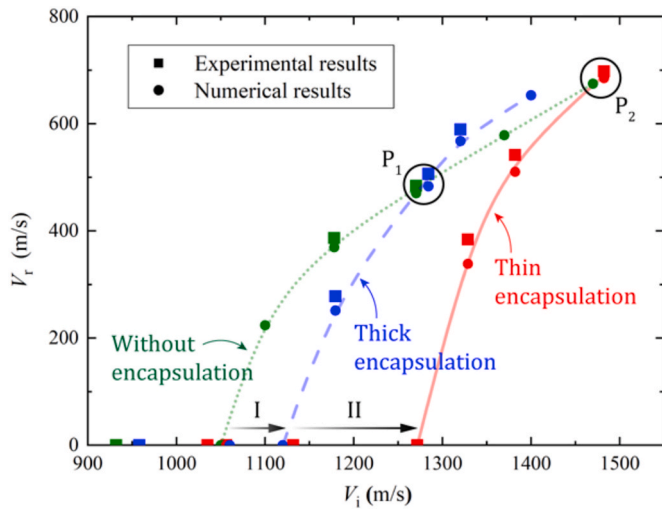
Fig. 8. Comparison between numerical predictions and experimental results of the bi-lay mosaic armors without encapsulation (C-w), with thin encapsulation (C-thin) and with thick encapsulation (C-thick).

encapsulation. Firstly, the influence of impact velocity on the ballistic performance of encapsulated Al plates (Series A) was investigated. Secondly, for specimens in Series C, different enhancements for encapsulated ceramic-metal mosaic armors with equal areal density were discussed. Finally, specimens with varying substructure ratios were compared to construct an optimal armor structure.

5.1. Enhancement mechanism

5.1.1. Influence of impact velocity

As shown in Figs. 7 and 8, when impacted at relatively low velocities (especially near the BLV), UHMWPE encapsulation led to great enhancement in ballistic resistance; however, with further increase in impact velocity, the residual velocity would gradually converge, for either the bare or encapsulated specimens. In other words, encapsulation could effectively increase the BLV of armors; but when the impact velocity exceeded the BLV, the enhancement of encapsulation decreased with increasing impact velocity.

Fig. 9 presented the simulated penetration process of UHMWPE encapsulated Al plate (A_1-E). Two typical impact velocities were selected: one was 1050 m/s (near the BLV) and the other was 1600 m/s. The penetration process could be divided into three stages. For the case of $V_i = 1050$ m/s shown in Fig. 9a, in the first stage, the front UHMWPE laminate was perforated in a few microseconds (0–8 μs), with only small deflection of the laminate attributed to the support of the Al plate; in the second stage, the Al plate began to fail in the mode of ductile hole enlargement (8–48 μs); after the inner Al plate was perforated, the spherical projectile directly impacted the rear UHMWPE and the penetration process started to enter the third stage (48–200 μs). While the first and second stages were similar in the two cases, the third stage for the case of $V_i = 1600$ m/s was significantly different from that of $V_i = 1050$ m/s. This difference was elucidated below.

For the case of $V_i = 1050$ m/s, the rear UHMWPE experienced large deflection deformation during the third stage, accompanied by serious delamination of sub-laminates. Meanwhile, the lateral UHMWPE was pulled from the edges to accommodate the transverse deflection of the rear encapsulation. This implied that the front, lateral and rear
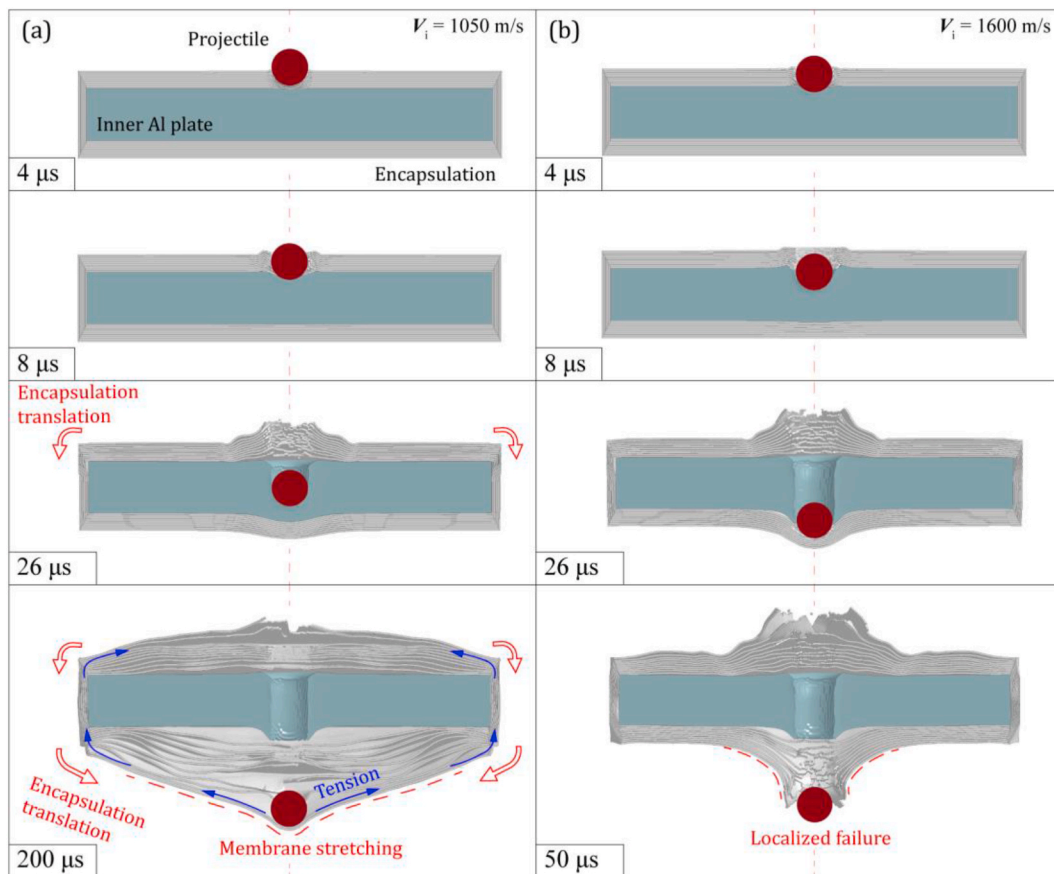

Fig. 9. Simulated penetration responses of UHMWPE encapsulated 30 mm Al plate (A_1-E, BLV was 1284 m/s) at impact velocity of (a) 1050 m/s and (b) 1600 m/s. The instant that the projectile initially impacted each target corresponded to 0 μs.
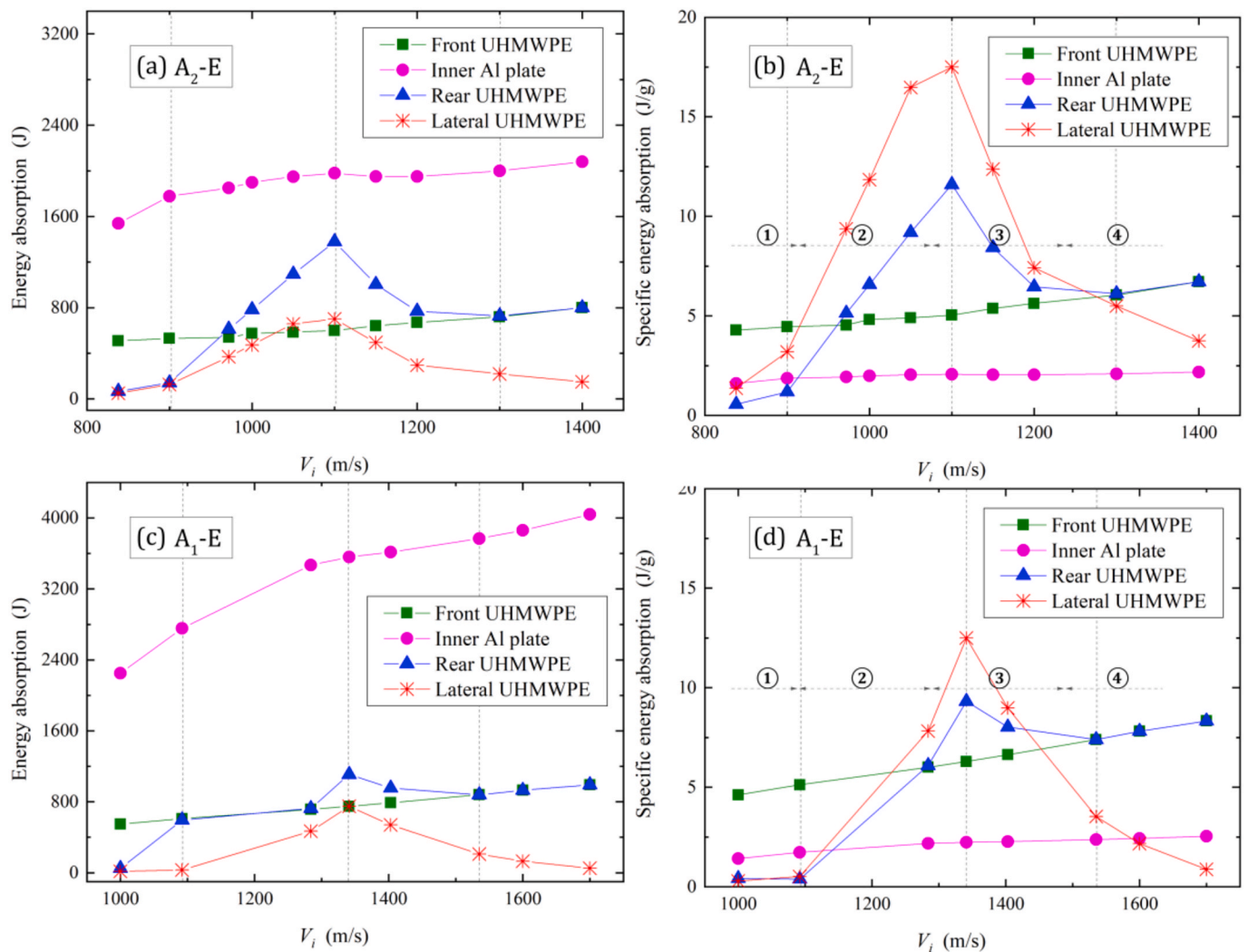
Fig. 10. Energy absorption and specific energy absorption of each substructure in encapsulated 18 mm Al plate (a, b) and encapsulated 30 mm Al plate (c, d) at selected impact velocities.

encapsulation materials resisted the projectile penetration as a whole. The encapsulation effect could efficiently disperse the localized impact loading to the entire structure, thus causing more energy to be dissipated. Differently, for the case of $V_i = 1600$ m/s, during the third stage, the projectile still had a large kinetic energy when it reached the rear UHMWPE. The projectile was therefore able to penetrate rapidly the rear UHMWPE laminate, causing shear plugging failure. Consequently, when the impact velocity was increased up to a certain value, the enhancement of UHMWPE encapsulation would disappear.

To explore how the enhancement of UHMPWE encapsulation varied with impact velocity, Fig. 10 compared the energy absorption (EA) and specific energy absorption (SEA) of each substructure at different impact velocities. Results demonstrated that the Al plate had the highest EA (Fig. 10a and c). Although the EA of the rear UHMPWE was low, its energy absorption efficiency (i.e., SEA) was high, especially at the impact velocity of ~1350 m/s (Fig. 10b and d). Noting that considering different densities, the ratio of internal energy to mass, i.e. SEA, was also added to compare the energy absorption efficiency of different substructures. For either the thin or thick Al plates, the EA and SEA exhibited the same variation trend as the impact velocity was increased.

With increasing impact velocity, the variation trend of SEA could be divided into 4 stages:

(1) In the first stage, the projectile was captured by the front UHMWPE and Al plate at relatively low impact velocities, with both the lateral and rear UHMWPE laminates barely participating in resisting the projectile.

(2) In the second stage, the SEA of the front UHMWPE increased slightly. For the lateral and rear UHMWPE, as the impact velocity was increased, the SEA dramatically increased to a peak (at the impact velocity near the BLV). Corresponding to Fig. 9a, translation and pull-in deformation of the lateral UHMWPE was obvious.

(3) In the third stage, the SEA of the lateral and rear UHMWPE decreased with the increase of impact velocity, which meant that less energy of the UHMWPE was dissipated. It was noteworthy that the enhancement, although gradually reduced, still existed.

(4) In the fourth stage, the SEA of the lateral UHMWPE returned to a low level, while the SEA of the rear UHMWPE almost equaled to that of the front one. The enhancement nearly disappeared at higher impact velocities, just like Fig. 9b.

It was worth noting that slightly higher EA and greater SEA of the rear and lateral UHMPWE was observed for the encapsulated thin Al plate (A$_2$-E), implying a larger contribution of encapsulation to its ballistic resistance.
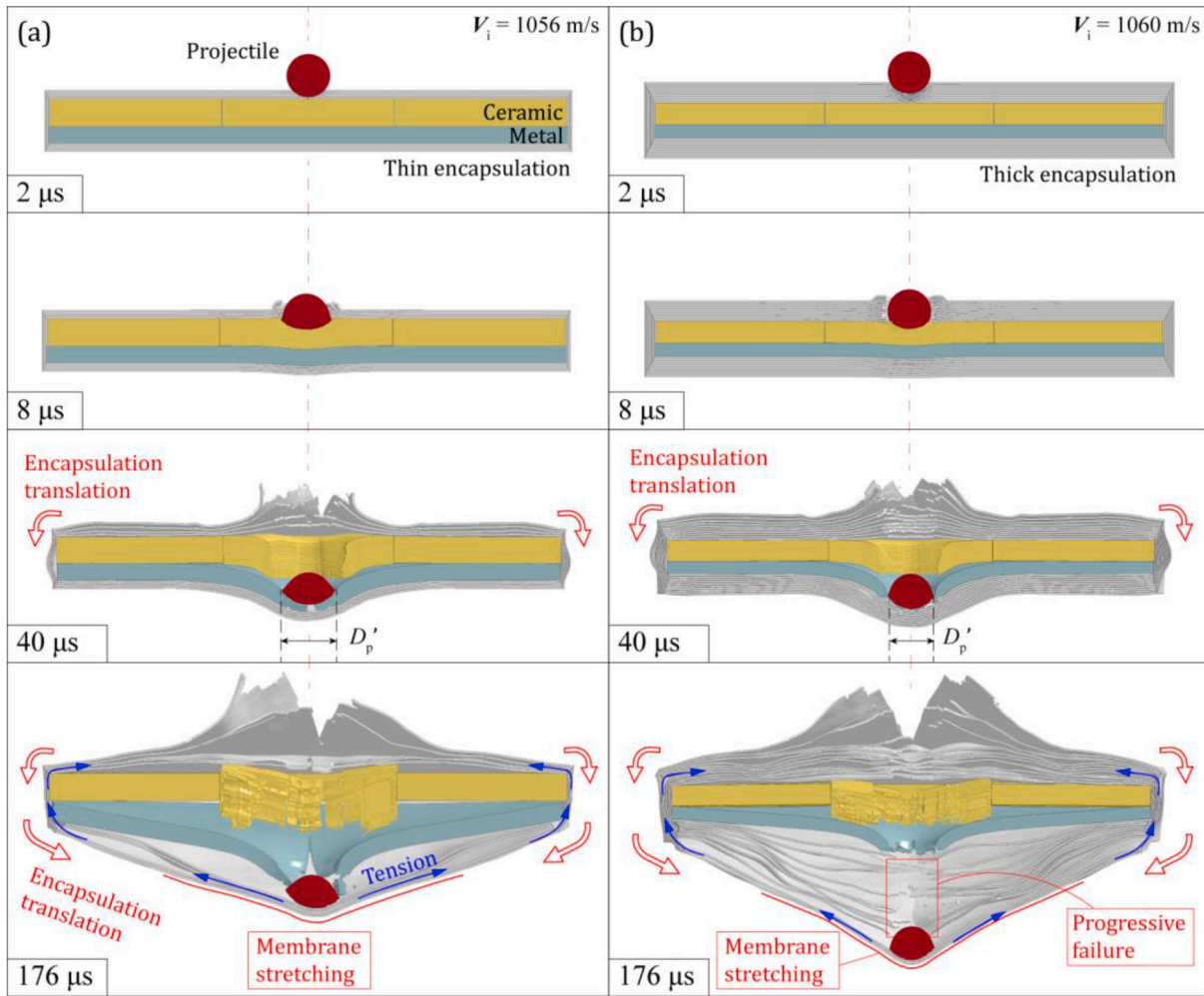
Fig. 11. Simulated penetration responses of encapsulated B$_4$C/Al plate with (a) thin and (b) thick encapsulation at similar impact velocities. $D_p^{'}$: diameter of deformed projectile.

5.1.2. Effect of substructure mass ratio

The results of Fig. 8 demonstrated that, with equal areal density, thin encapsulation specimens exhibited better ballistic resistance than the thick ones. To explore the influence of armor substructures, Fig. 11 compared the calculated penetration responses of encapsulated B$_4$C/Al plate having thin and thick encapsulations. In general, the penetration processes exhibited similar enhancement mechanisms, suggesting that the encapsulation enhancement mechanism was unrelated to armor inner substructures. However, the enhancement effect was different due to the different defense mechanism of each substructure.

As illustrated in Fig. 11, different arrangements of the mass ratio between the ceramic and the UHMWPE led to different ballistic performances. On one hand, the specimen with a relatively high mass ratio of ceramic (like Fig. 11a) could deform and fragment the projectile more

effectively (*i.e.*, larger diameter $D_p^{'}$ of deformed projectile), induce more plastic deformation of the Al plate (*i.e.*, plastic deformation within a larger area), and prevent premature failure beneath the impact (*i.e.*, membrane stretching without failure). On the contrary, the specimen with a lower ceramic mass ratio (Fig. 11b) failed in a progressive manner, accompanied with membrane stretching. Similar phenomena were also observed during experiment, as shown in Fig. 4a. For encapsulated specimens (*i.e.*, C-thin and C-thick), it should be noticed that the front UHMWPE worked as a relatively soft surface, resulting in limited projectile deformation. However, in terms of ballistic resistance, the encapsulated C-thin and C-thick were superior to the unencapsulated C-w (*i.e.*, the traditional bi-layer ceramic/metal armor), mainly attributed to the energy dissipated by the lateral and rear UHMWPE encapsulations via serious stretching deformation.

Table 7

Six combinations of the mass (or thickness) ratio of B$_4$C ceramic tile, Al plate and UHMWPE encapsulation.

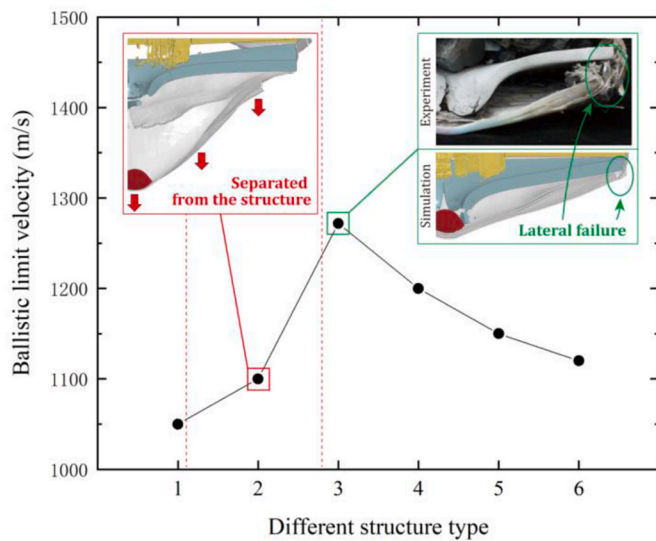| NO.	Thickness (mm)				Mass ratio		
	B$_4$C	Al	UHMWPE	Total thickness	B$_4$C	Al	UHMWPE
1	8.5	6	**0**	14.5	56.74%	43.26%	0.00%
2	8	6	**1.2**	14	51.98%	42.10%	5.93%
3	8	5	**2.4**	13	52.55%	35.47%	11.98%
4	8	4	**3.6**	12	53.13%	28.69%	18.17%
5	6.5	5	**4.2**	11.5	43.07%	35.78%	21.15%
6	6.5	4	**6**	10.5	42.26%	28.09%	29.65%

Fig. 12. Ballistic limit velocities for six different arrangements of substructure mass ratio.

5.2. Optimal design of the substructure mass ratios

To balance the mass ratio of the UHMWPE encapsulation, the B_4C ceramic tile, and the Al plate, a preliminary optimal design was performed for maximum BLV. As summarized in Table 7, six thickness combinations of B_4C ceramic tile, Al plate and UHMWPE encapsulation were simulated, with the total mass of each specimen fixed at the same value. The simulation results were presented in Fig. 12.

It was seen from Fig. 12 that the BLV of an encapsulated armor depended significantly upon its substructure configuration, with the highest BLV achieved by Specimen 3 with an encapsulation thickness of 2.4 mm and a mass ratio of 11.98%. For Specimen 2, the encapsulation was too thin to maintain a stable connection, and its lateral UHMWPE failed early during the interaction between projectile and rear UHMWPE. Subsequently, the rear UHMWPE separated from the structure and flew away together with the projectile like in a free boundary condition (red frame in Fig. 12), thus contributing little to resist the projectile. As for Specimen 3, although a few inner layers of its lateral UHMWPE failed, the outer layers were strong enough to accommodate the large deflection of the rear UHMWPE (green frame of Fig. 12). For specimens with an encapsulation thickness exceeding 2.4 mm, as the encapsulation thickness was increased, the BLV decreased monotonically. This implied that there existed an optimal thickness or mass ratio of UHMWPE encapsulation for maximum enhancement in ballistic resistance.

6. Conclusions

A combined experimental and numerical approach had been employed to investigate how UHMWPE encapsulation affected the ballistic performance of bi-layer mosaic armors. Three series of specimens were prepared and tested through ballistic experiments. The influences of impact velocity and substructure mass ratio as well as the enhancement mechanisms underlying UHMWPE encapsulation were systematically investigated. Main conclusions were summarized as follows.

(1) Encapsulation could efficiently improve the ballistic limit velocity (BLV) of traditional bi-layer armors: in the presence of lateral encapsulation, the front and rear UHMWPE encapsulations could resist the projectile as a whole to disperse the localized impact to the entire structure.

(2) When impacted at a relatively low velocity (especially near the BLV), UHMWPE encapsulation could lead to a dramatic raise in ballistic resistance. However, the enhancement gradually disappeared as the impact velocity was increased: when impacted at a velocity exceeding the BLV, the damage was much localized and the UHMWPE encapsulation was penetrated by the projectile.

(3) The inner substructure of armor greatly affected the enhancement effect of UHMWPE encapsulation. Encapsulated bi-layer ceramic/metal plates exhibited better ballistic resistance than encapsulated metal plates.

(4) The UHMWPE encapsulation and the ceramic tiles mainly contributed to energy dissipation and projectile deformation, respectively. For maximum ballistic resistance, the mass ratio of armor substructures (e.g., UHMWPE encapsulation, ceramic tile and metal plate) needed to be optimized according to specific protection requirement.

Author statement

Zhong-Nan Zhao: Conceptualization, Methodology, Software, Validation, Formal analysis, Investigation, Data Curation, Writing - Original Draft, Writing - Review & Editing, Visualization.
Bin Han: Resources, Writing - Review & Editing, Supervision, Project administration.
Rui Zhang: Software, Validation.
Qi Zhang: Resources.
Qian-Cheng Zhang: Resources.
Chang-Ye Ni: Software.
Tian Jian Lu: Resources, Writing - Review & Editing, Supervision, Project administration, Funding acquisition.

Declaration of competing interest

The authors declare that they have no known competing financial interests or personal relationships that could have appeared to influence the work reported in this paper.

References

[1] Wilkins ML, Cline CF, Honodel CA. Fourth progress report of light armor program. Livermore: California Univ.; 1969. Lawrence Radiation Lab.
[2] Wilkins ML. Mechanics of penetration and perforation. Int J Eng Sci 1978;16(11): 793–807.
[3] Han B, Zhang Z-J, Zhang Q-C, Zhang Q, Lu TJ, Lu B-H. Recent advances in hybrid lattice-cored sandwiches for enhanced multifunctional performance. Extreme Mechanics Letters 2017;10:58–69.
[4] Zhang R, Han B, Li L, Zhao Z-N, Zhang Q, Zhang Q-C, et al. Influence of prestress on ballistic performance of bi-layer ceramic composite armors: experiments and simulations. Compos Struct 2019;227:111258–62.
[5] Yang M, Han B, Su P-B, Wei Z-H, Zhang Q, Zhang Q-C, et al. Free vibration and axial compression of all-metallic cylindrical and truncated conical sandwich shells with corrugated cores. J Sandw Struct Mater 2020:10996.
[6] Shokrieh MM, Javadpour GH. Penetration analysis of a projectile in ceramic composite armor. Compos Struct 2008;82(2):269–76.
[7] Übeyli M, Yıldırım RO, Ögel B. Investigation on the ballistic behavior of Al2O3/ Al2024 laminated composites. J Mater Process Technol 2008;196(1):356–64.
[8] Ernst H-J, Wiesner V, Wolf T. Armor ceramics under high-velocity impact of a medium-caliber long-rod penetrator. Ceram Trans 2002;134:23–31.

[9] Yin Z, Yuan J, Chen M, Si D, Xu C. Mechanical property and ballistic resistance of graphene platelets/B4C ceramic armor prepared by spark plasma sintering. Ceram Int 2019;45(17):23781–7.

[10] Hazell PJ, Roberson CJ, Moutinho M. The design of mosaic armour: the influence of tile size on ballistic performance. Mater Des 2008;29(8):1497–503.

[11] Ni CY, Li YC, Xin FX, Jin F, Lu TJ. Ballistic resistance of hybrid-cored sandwich plates: numerical and experimental assessment. Compos Appl Sci Manuf 2013;46: 69–79.

[12] Zhao Z-N, Han B, Li F-H, Zhang R, Su P-B, Yang M, et al. Enhanced bi-layer mosaic armor: experiments and simulation. Ceram Int 2020;46(15):23854–66.

[13] Yu R-P, Wang X, Zhang Q-C, Li L, He S-Y, Han B, et al. Effects of sand filling on the dynamic response of corrugated core sandwich beams under foam projectile impact. Compos B Eng 2020;197:108135.

[14] Karthikeyan K, Russell BP, Fleck NA, O'Masta M, Wadley HNG, Deshpande VS. The soft impact response of composite laminate beams. Int J Impact Eng 2013;60: 24–36.

[15] Yu B, Karthikeyan K, Deshpande VS, Fleck NA. Perforation resistance of CFRP beams to quasi-static and ballistic loading: the role of matrix strength. Int J Impact Eng 2017;108:389–401.

[16] Rao MP, Duan Y, Keefe M, Powers BM, Bogetti TA. Modeling the effects of yarn material properties and friction on the ballistic impact of a plain-weave fabric. Compos Struct 2009;89(4):556–66.

[17] Phoenix SL, Yavuz AK, Porwal PK. New interference approach for ballistic impact into stacked flexible composite body armor. AIAA J 2010;48(2):490–501.

[18] Porwal PK, Phoenix SL. Modeling system effects in ballistic impact into multi-layered fibrous materials for soft body armor. Int J Fract 2005;135(1):217–49.

[19] Phoenix SL, Porwal PK. A new membrane model for the ballistic impact response and V50 performance of multi-ply fibrous systems. Int J Solid Struct 2003;40(24): 6723–65.

[20] Greenhalgh ES, Bloodworth VM, Iannucci L, Pope D. Fractographic observations on Dyneema® composites under ballistic impact. Compos Appl Sci Manuf 2013;44: 51–62.

[21] Russell BP, Karthikeyan K, Deshpande VS, Fleck NA. The high strain rate response of Ultra High Molecular-weight Polyethylene: from fibre to laminate. Int J Impact Eng 2013;60:1–9.

[22] Dasgupta K. Role of carbon nanotubes in the ballistic properties of boron carbide/carbon nanotube/ultrahigh molecular weight polyethylene composite armor. Ceram Int 2020;46(4):4137–41.

[23] Zhang R, Qiang L-S, Han B, Zhong J-Y, Qiang L-S, Ni C-Y, et al. Enhanced ballistic resistance of multilayered cross-ply UHMWPE laminated plates. Compos Sci Technol 2020. submitted for publication.

[24] Cunniff PM. Dimensionless parameters for optimization of textile-based body armor systems. In: Proceedings of the 18th international symposium on ballistics. San Antonio, TX, USA: Technomic Publishing Company Inc Lancaster PA; 1999. p. 1303–10.

[25] Babiker DMD, Wan C, Mansoor B, et al. Superior lithium battery separator with extraordinary electrochemical performance and thermal stability based on hybrid

UHMWPE/SiO2 nanocomposites via the scalable biaxial stretching process. Compos B Eng 2021;211:108658.

[26] Rodrigues MM, Fontoura CP, Maddalozzo AED, et al. Ti, Zr and Ta coated UHMWPE aiming surface improvement for biomedical purposes. Compos B Eng 2020;189:107909.

[27] Di Maro M, Duraccio D, Malucelli G, et al. High density polyethylene composites containing alumina-toughened zirconia particles: Mechanical and tribological behavior. Compos B Eng 2021:108892.

[28] Hu D, Zhang Y, Shen Z, Cai Q. Investigation on the ballistic behavior of mosaic SiC/UHMWPE composite armor systems. Ceram Int 2017;43(13):10368–76.

[29] Yan LL, Yu B, Han Ba, Zhang QC, Lu TJ, Lu BH. Effects of aluminum foam filling on the low-velocity impact response of sandwich panels with corrugated cores. J Sandw Struct Mater 2020;22(4):929–47.

[30] Zhang R, Han B, Lu TJ. Confinement effects on compressive and ballistic performance of ceramics: a review. Int Mater Rev 2020;1(1):1–26.

[31] Shanmugam L, Kazemi ME, Rao Z, Yang L, Yang J. On the metal thermoplastic composite interface of Ti alloy/UHMWPE-Elium® laminates. Compos B Eng 2020; 181:107578.

[32] Rezaie AB, Liebscher M, Ranjbarian M, et al. Enhancing the interfacial bonding between PE fibers and cementitious matrices through polydopamine surface modification. Compos B Eng 2021;217:108817.

[33] Nguyen LH, Lässig TR, Ryan S, Riedel W, Mouritz AP, Orifici AC. A methodology for hydrocode analysis of ultra-high molecular weight polyethylene composite under ballistic impact. Compos Appl Sci Manuf 2016;84:224–35.

[34] Zhang R, Qiang L-S, Han B, Zhao Z-Y, Zhang Q-C, Ni C-Y, et al. Ballistic performance of UHMWPE laminated plates and UHMWPE encapsulated aluminum structures: numerical simulation. Compos Struct 2020;252:112686.

[35] O'Masta MR, Deshpande VS, Wadley HNG. Mechanisms of projectile penetration in Dyneema® encapsulated aluminum structures. Int J Impact Eng 2014;74:16–35.

[36] O'Masta MR, Compton BG, Gamble EA, Zok FW, Deshpande VS, Wadley HNG. Ballistic impact response of an UHMWPE fiber reinforced laminate encasing of an aluminum-alumina hybrid panel. Int J Impact Eng 2015;86:131–44.

[37] Hazzard MK, Trask RS, Heisserer U, Van Der Kamp M, Hallett SR. Finite element modelling of Dyneema® composites: from quasi-static rates to ballistic impact. Compos Appl Sci Manuf 2018;115:31–45.

[38] Phoenix SL, Heisserer U, Van der Werff H, Van der Jagt-Deutekom M. Modeling and experiments on ballistic impact into UHMWPE yarns using flat and saddle-nosed projectiles. Fibers 2017;5(1):8.

[39] Johnson GR, Cook WH. Fracture characteristics of 3 metals subjected to various strains, strain rates, temperatures and pressures. Eng Fract Mech 1985;21(1): 31–48.

[40] Brar NS, Joshi VS, Harris BW, Elert M, Furnish MD, Anderson WW, et al. Constitutive model constants for Al7075-T651 and Al7075-T6. In: AIP conference proceedings; 2009. p. 945–8.

[41] Hajializadeh F, Mashhadi MM. Investigation and numerical analysis of impulsive hydroforming of aluminum 6061-T6 tube. J Manuf Process 2015;20:257–73.

[42] Johnson GR, Holmquist TJ. Response of boron carbide subjected to large strains, high strain rates, and high pressures. J Appl Phys 1999;85(12):8060–73.